

Cu-Mn-Co oxides as protective materials in SOFC technology: The effect of chemical composition on mechanochemical synthesis, sintering behaviour, thermal expansion and electrical conductivity

Masi, Andrea; Bellusci, Mariangela; McPhail, Stephen J.; Padella, Franco; Reale, Priscilla; Hong, Jong-Eun; Steinberger-Wilckens, Robert; Carlini, Maurizio

DOI:

[10.1016/j.jeurceramsoc.2016.09.025](https://doi.org/10.1016/j.jeurceramsoc.2016.09.025)

License:

Creative Commons: Attribution-NonCommercial-NoDerivs (CC BY-NC-ND)

Document Version

Peer reviewed version

Citation for published version (Harvard):

Masi, A, Bellusci, M, McPhail, SJ, Padella, F, Reale, P, Hong, J-E, Steinberger-Wilckens, R & Carlini, M 2017, 'Cu-Mn-Co oxides as protective materials in SOFC technology: The effect of chemical composition on mechanochemical synthesis, sintering behaviour, thermal expansion and electrical conductivity', *Journal of the European Ceramic Society*, vol. 37, no. 2, JECS-10852, pp. 661–669. <https://doi.org/10.1016/j.jeurceramsoc.2016.09.025>

[Link to publication on Research at Birmingham portal](#)

General rights

Unless a licence is specified above, all rights (including copyright and moral rights) in this document are retained by the authors and/or the copyright holders. The express permission of the copyright holder must be obtained for any use of this material other than for purposes permitted by law.

- Users may freely distribute the URL that is used to identify this publication.
- Users may download and/or print one copy of the publication from the University of Birmingham research portal for the purpose of private study or non-commercial research.
- User may use extracts from the document in line with the concept of 'fair dealing' under the Copyright, Designs and Patents Act 1988 (?)
- Users may not further distribute the material nor use it for the purposes of commercial gain.

Where a licence is displayed above, please note the terms and conditions of the licence govern your use of this document.

When citing, please reference the published version.

Take down policy

While the University of Birmingham exercises care and attention in making items available there are rare occasions when an item has been uploaded in error or has been deemed to be commercially or otherwise sensitive.

If you believe that this is the case for this document, please contact UBIRA@lists.bham.ac.uk providing details and we will remove access to the work immediately and investigate.

1 **Cu-Mn-Co oxides as Protective Materials in SOFC Technology: the Effect of Chemical**
2 **Composition on Mechanochemical Synthesis, Sintering Behaviour, Thermal Expansion and**
3 **Electrical Conductivity**

4

5 Andrea Masi 1-3, Mariangela Bellusci 1, Stephen McPhail 1, Franco Padella 1, Priscilla Reale 1,
6 Jong-Eun Hong 2, Robert Steinberger-Wilckens 2, Maurizio Carlini 3

7 1) ENEA C.R. Casaccia, 00123 Rome, Italy

8 2) School of Chemical Engineering, University of Birmingham, Edgbaston, Birmingham B15 2TT,
9 UK

10 3) University of Tuscia - DAFNE, 01100 Viterbo, Italy

11 **Abstract**

12 To study the effect of the composition on the physico-chemical properties of mixed Cu-Mn-Co
13 oxides as SOFC interconnects coating materials, different compounds have been obtained through a
14 High Energy Ball Milling (HEBM) process. The mechanochemical treatment produces highly
15 activated multi-phase powders that easily react at intermediate temperature to form the equilibrium
16 products. Thermogravimetric, dilatometric and in-situ high temperature analyses allowed to show
17 that Copper addition promotes cubic spinel stability at low temperature and enhances sintering
18 behaviour.

19 Dilatometric and conductivity analysis carried out on sintered pellets allowed to obtain simple
20 relations between the materials properties and the composition. Coefficient of Thermal Expansion
21 (CTE) and electrical conductivity are increased by Copper doping and high Co:Mn ratios. These
22 findings suggest that the materials characteristics can be opportunely tuned through appropriate
23 composition design, to simultaneously obtain enhanced sintering behaviour, high electrical
24 conductivity and CTE adapted to match the substrate.

25

- 26 Keywords
- 27 Spinel oxides;
- 28 Ball Milling;
- 29 Thermal Expansion;
- 30 Solid Oxide Fuel Cell;
- 31 Interconnect Coating.

32 1. Introduction:

33 Solid Oxide Fuel Cells (SOFCs) represent promising energy conversion devices characterized by
34 high efficiency and virtually absent polluting emissions. To achieve high power required for
35 practical use, the cells are assembled in series to obtain stacks, and a crucial part for the stack
36 design is represented by the cell interconnect. Its role is to separate cathode and anode side of
37 adjacent cells maintaining electrical link and granting structural stability and support. Mechanical
38 compatibility, chemical stability, gas impermeability and high electrical conductivity are needed for
39 proper functionality.

40 In the last decade, research on cell materials permitted to lower operating temperatures below
41 800°C, allowing to design stacks with metallic interconnects characterized by reduced costs and
42 enhanced processability with respect to traditional ceramic parts. Among the metal alloys, Cr-rich
43 ferritic stainless steels possess the Coefficient of Thermal Expansion (CTE) compatibility with
44 SOFC materials, and low cost requirements needed for mass production. In operating environment
45 these alloys undergo however severe corrosion issues, resulting in significant degradation of cell
46 performances. The growth of superficial chromium-rich oxides, besides lowering electrical
47 conductivity, leads in fact to significant chrome volatilization and its subsequent reaction with
48 cathode materials, lowering the cathode active area. Protective coatings that grant electrical
49 conductivity for long term application, inhibiting Cr volatilization, are therefore required[1,2].

50 For this purpose, Mn-Co spinels have been suggested as best candidates, due to their high electrical
51 conductivity and thermal expansion compatibility with ferritic alloys [3]. The composition and
52 thermal history of these compounds influence directly the reticular structure and the chemico-
53 physical properties of the materials [4,5], and several studies have been carried out to further tune
54 mechanical compatibility or electrical properties. The addition of transition metals or reactive
55 elements such as Fe, Ti, Cu, Ni or Y has been evaluated, preparing powders and coating with
56 several methods [6–9]. In particular, it has been observed that the composition affects the thermal
57 expansion behaviour of the compound, and several studies include dilatometric analyses on doped

58 or undoped Mn-Co spinels [3,7,9–15]. While some indications on how chemical composition
59 affects CTE can be deduced (with high Mn, Fe or Ti content decreasing CTE [12] or Ni and Cu
60 increasing CTE [7,9,16]) no clear relation between dopant amount and CTE can be inferred due to
61 significant scattering of the reported results.

62 In our previous work, we have evaluated High Energy Ball Milling (HEBM) as synthesis technique
63 of mixed Mn-Co spinels starting from Mn and Co oxides [17]. HEBM is a mechanochemical
64 technique in which the kinetic energy of colliding balls is transferred to powders trapped against the
65 vial walls. The energy transfer, beside producing comminution and nanostructuring of the
66 powders, promotes interdiffusion of the different chemical elements, atomic rearrangements,
67 nucleation of new phases and other phenomena [18]. Due to the impulsive nature of the energy
68 transfer mechanism, occurring near room temperature, the products are often characterized by
69 metastable phases and highly reactive behaviour [19–21]. In our explorative work we observed that
70 to complete the mechanochemical solid state reaction of Mn and Co oxides, long mechanochemical
71 treatments are needed, but short milling times (i.e. 10 hours) are effective to obtain a highly reactive
72 multi-phase powder. The milled powder can easily form in-situ the equilibrium products during
73 sintering treatments. HEBM is therefore proposed as potential substitute of the high temperature
74 solid state reaction synthesis usually exploited to produce these mixed oxides.

75 In this work, different Mn-Co and Cu-Mn-Co oxide mixtures have been subjected to a short HEBM
76 treatment to prepare spinels characterized by different chemical composition. The compositions
77 were chosen to evaluate how different Mn:Co ratios, possibly in presence of copper, can affect the
78 materials response to the mechanochemical treatment and its properties when exposed to high
79 temperature. High temperature phases evolution, phase stability and sintering behaviour of the
80 treated powder have been studied by means of thermogravimetric analysis, in-situ high temperature
81 X-Ray Diffraction (XRD) and dilatometric measurements. Also the effect of the composition on
82 thermal expansion and electrical conductivity has been evaluated and discussed.

83

84 2. Experimental Procedure

85 The HEBM treatment was carried out using a SPEX8000M mixer mill, cylindrical steel vials (60
 86 cm³ volume) and steel balls (10mm diameter) for 10 hours. Stoichiometric amounts of Mn₃O₄
 87 (Sigma Aldrich, 97%), Co₃O₄ (Sigma Aldrich, 99%) and CuO (Carlo Erba, 99%) were mixed in
 88 order to obtain the samples with composition reported in Table 1. A powder to balls weight ratio of
 89 1:10 was used for the experiments; vials were loaded with 8g of powders and sealed under argon
 90 atmosphere.

91

92 *Table 1: Sample nomenclature and nominal composition:*

Sample name	Metal ratio			Corresponding composition
	Mn	Co	Cu	
MnCo2	0.33	0.67		MnCo ₂ O ₄
Mn1.25Co1.75	0.42	0.58		Mn _{1.25} Co _{1.75} O ₄
Mn1.5Co1.5	0.50	0.50		Mn _{1.5} Co _{1.5} O ₄
Mn1.33Co1.17Cu0.5	0.44	0.39	0.17	Mn _{1.33} Co _{1.17} Cu _{0.5} O ₄
Mn1.58Co0.93Cu0.5	0.52	0.31	0.17	Mn _{1.57} Co _{0.93} Cu _{0.5} O ₄
Mn2.05Co0.45Cu0.5	0.68	0.15	0.17	Mn _{2.05} Co _{0.45} Cu _{0.5} O ₄

93

94 A 120° angular dispersion X-ray diffractometer (XRD3000 from Italstructure, curved PSD detector
 95 from INEL), equipped with Fe K_{α1} radiation source, was used to perform X-Ray diffraction analysis
 96 (XRD). Phase identification was performed on collected patterns using the PDF-2 database[22] as
 97 reference data. Lorentzian fitting of selected reflections allowed to evaluate cell parameters and to
 98 calculate accordingly theoretical densities, considering nominal compositions of the samples. In situ
 99 high temperature measurements were performed installing a heating reactive chamber (Anton Paar

100 Gmbh, Graz, Austria). The measurements were carried out in air, at heating and cooling rates of
101 10°C/min, 300 s of thermal equilibrium time before the measurements and 300 s of acquisition
102 time.

103 Scanning Electron Mycroscopy (SEM) analyses were carried out on a Hitachi TM3030Plus SEM
104 equipped with EDX energy-dispersive X-ray (EDX) microanalysis.

105 N₂ adsorption at 77K technique (Quantachrome Autosorb-iQ) was exploited to evaluate mean
106 particle size. Specific Surface Area (SSA) was calculated applying the BET method[23]. Average
107 particle size was calculated assuming spherical particle shape.

108 Thermogravimetric analyses were carried out in air using a Pyris Diamond TG/DTA (Perkin
109 Elmer), heating the samples up to 1200°C at 5°C/min, followed by 60 minutes of high temperature
110 dwell time and cooling to room temperature at 5°C/min.

111 Dilatometric measurements were carried out using a push-rod dilatometer (DIL 402 C, NETZSCH).

112 To evaluate sintering behaviour, consolidated pellets of about 6mm diameter were obtained by
113 uniaxial cold pressing (3.5 T/cm²). The experiments were carried out heating at 5°C/min scan rate
114 up to 1200°C. To measure thermal expansion, experiments were carried out on pellets of about
115 6mm diameter and 2.5mm height sintered as described later in the text. The measurements were
116 carried out with a heating rate of 10°C/min. Average CTE was calculated between room
117 temperature and 800°C as: $CTE = \frac{1}{L_0} \frac{\Delta L}{\Delta T}$, where L_0 represents the initial length and ΔL the length
118 change occurring in the ΔT temperature range.

119 Electrical conductivity was estimated by applying the Van der Pauw method [24] on pellets of
120 about 10mm diameter, obtained by uniaxial cold pressing (3.5 T/cm²) and successive sintering (see
121 below for experimental details). The 500-800°C temperature range was investigated, using a
122 PAR273A potentiostat coupled to a HP 3457A multimeter. Activation energy E_a was calculated
123 from the Arrhenius plot obtained using the formula: $\sigma = \frac{\sigma_0}{T} e^{-\frac{E_a}{kT}}$, with σ electrical conductivity, T
124 temperature, σ_0 pre-exponential factor, E_a activation energy and k Boltzmann's constant.

125 3. Results and discussion

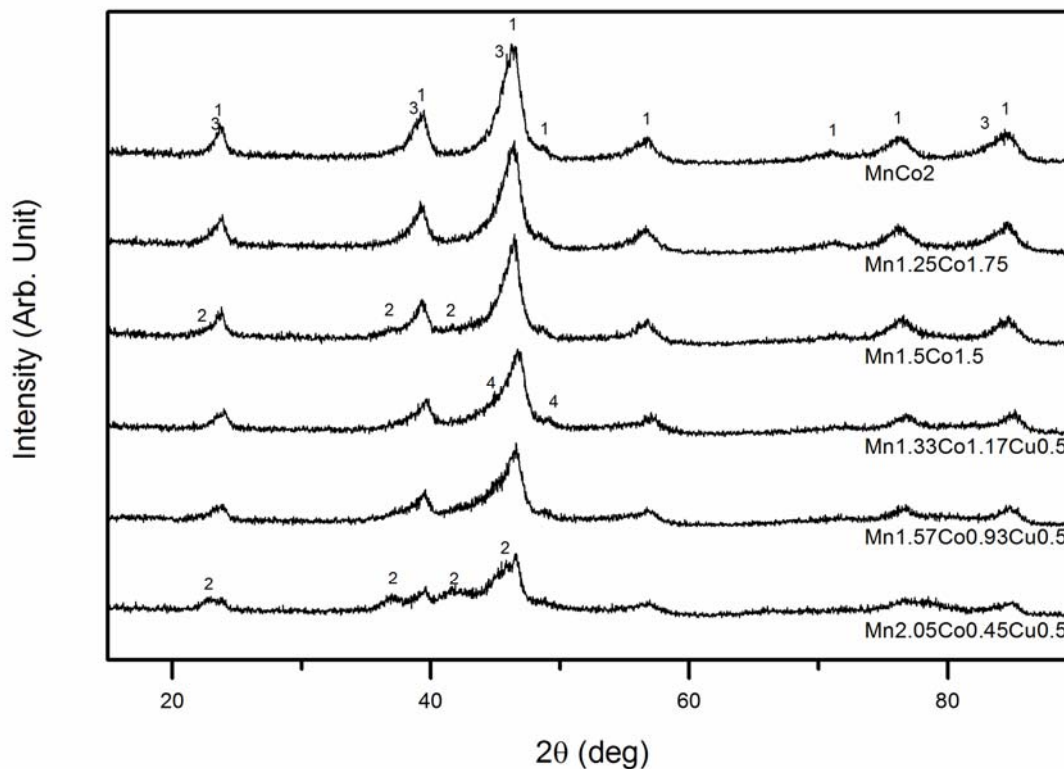
126 3.1. Powder characterization

127 The mechanochemical treatment produces fine black powders. After the milling treatments, EDX
128 analyses have been successfully carried out to exclude the presence of iron and chromium that
129 could highlight chemical contamination from the milling equipment. In Fig. 1 are reported the XRD
130 patterns of the samples after 10 hours of milling. Significant peak broadening can be observed due
131 to nanostructuring of diffractive domains and lattice defectivity induced by the HEBM treatment.
132 The three Mn-Co samples evidence the residual presence of the Co_3O_4 precursor phase (JCPDS
133 card n. 42-1467). The observed asymmetry towards lower angles can be related to the nucleation of
134 a mixed MnCo_2O_4 phase (JCPDS card n. 23-1237). Only the $\text{Mn}_{1.5}\text{Co}_{1.5}$ sample shows signals
135 related to the Mn_3O_4 precursor phase (JCPDS card n. 24-0734).

136 Cu-containing samples show similar peak broadening. The $\text{Mn}_{1.33}\text{Co}_{1.17}\text{Cu}_{0.5}$ pattern exhibits
137 mainly reflections compatible with the Co_3O_4 phase, with the already observed asymmetry towards
138 lower angles. Small broadened peaks at $2\theta \cong 45$ and $2\theta \cong 49$ degrees are ascribable to the presence of
139 CuO phase (JCPDS card n. 48-1548). Raising Mn content, reflections related to Mn_3O_4 become
140 evident, similarly to what was observed for the Mn-Co samples.

141 The higher stability exhibited by the cobalt precursor phase in comparison with to the Mn and Cu
142 oxides with respect the mechanochemical action is clearly evident from these results. The
143 $\text{Mn}_{1.5}\text{Co}_{1.5}$ sample, composed by similar Co and Mn amounts, is characterized by Mn_3O_4
144 reflections scarcely visible with respect to the cubic Co_3O_4 phase peaks. Regarding copper oxide, it
145 can be clearly observed from the pattern related to the $\text{Mn}_{2.05}\text{Co}_{0.45}\text{Cu}_{0.5}$ sample, that also the
146 CuO phase gets easily destructured during the milling, the CuO peaks being significantly lower and
147 broader with respect to those of cobalt oxide. The observed phenomena can be ascribed to the
148 difference in hardness of the materials, with Co spinel characterized by significantly higher
149 hardness with respect to Hausmannite (Mohs hardness: 5.5) [25] and Tenorite (Mohs hardness:

150 3.5-4). The successive deconstruction of the crystalline phases easily promotes interdiffusion of Mn
 151 and Cu atoms in the Co precursors phase or in the nucleating mixed spinel lattice.
 152



153
 154 *Fig. 1. X-ray powder diffraction patterns of the different samples after 10h of milling; 1) Co_3O_4 2) Mn_3O_4)*
 155 *$MnCo_2O_4$ 4) CuO reflections.*

156
 157 In Table 2 BET specific surface area and calculated mean particle size are reported. All the samples
 158 exhibit comparable values, with Copper-containing powders characterized by the lower BET area,
 159 suggesting that Copper addition promotes higher aggregation degree. Mean particle size ranges
 160 between 170 and 330nm.

161
 162 *Table 2: BET surface area and BET particle size for the 10h HEBM powders:*

Sample	BET	I^*
--------	-----	-------

	(m ² /g)	(nm)
MnCo2	6.2±0.3	176±9
Mn1.25Co1.75	5.7±0.3	195±10
Mn1.5Co1.5	4.5±0.2	255±12
Mn1.33Co1.17Cu0.5	4.2±0.2	265±13
Mn1.57Co0.93Cu0.5	3.5±0.2	325±15
Mn2.05Co0.45Cu0.5	4.1±0.2	293±13

$$*l = \frac{6}{A_{BET} \cdot \rho}$$

163

164 In order to evaluate how the different Mn:Co ratios and the Cu addition influence the high
 165 temperature properties of the samples, the milled powders were subjected to thermogravimetric
 166 analysis. In Fig. 2 thermogravimetric analysis curves are reported. All samples show a weight loss
 167 step ascribable to the departure of adsorbed humidity. In the 200-500°C temperature range, a
 168 gradual weight increase can be observed for all compositions. The effectiveness of
 169 mechanochemical activation can be recognized from this phenomenon: the HEBM treatment
 170 promotes in fact high degree of interdiffusion of the starting oxides, and being carried out in Ar
 171 atmosphere it is likely to create anion defective lattices. The highly defective and nanostructured
 172 powders will easily react at low temperature with oxygen, most likely leading to the oxidation of
 173 Mn to higher oxidation states. The low cation mobility at low temperature does not however allow
 174 major lattice rearrangement, producing metastable non-stoichiometric compounds. Similar
 175 metastable mixed valence spinels have been already observed for transition metal oxide systems,
 176 although prepared by other routes, and their formation was related to a high reactivity associated
 177 with highly nanostructured compounds [26].

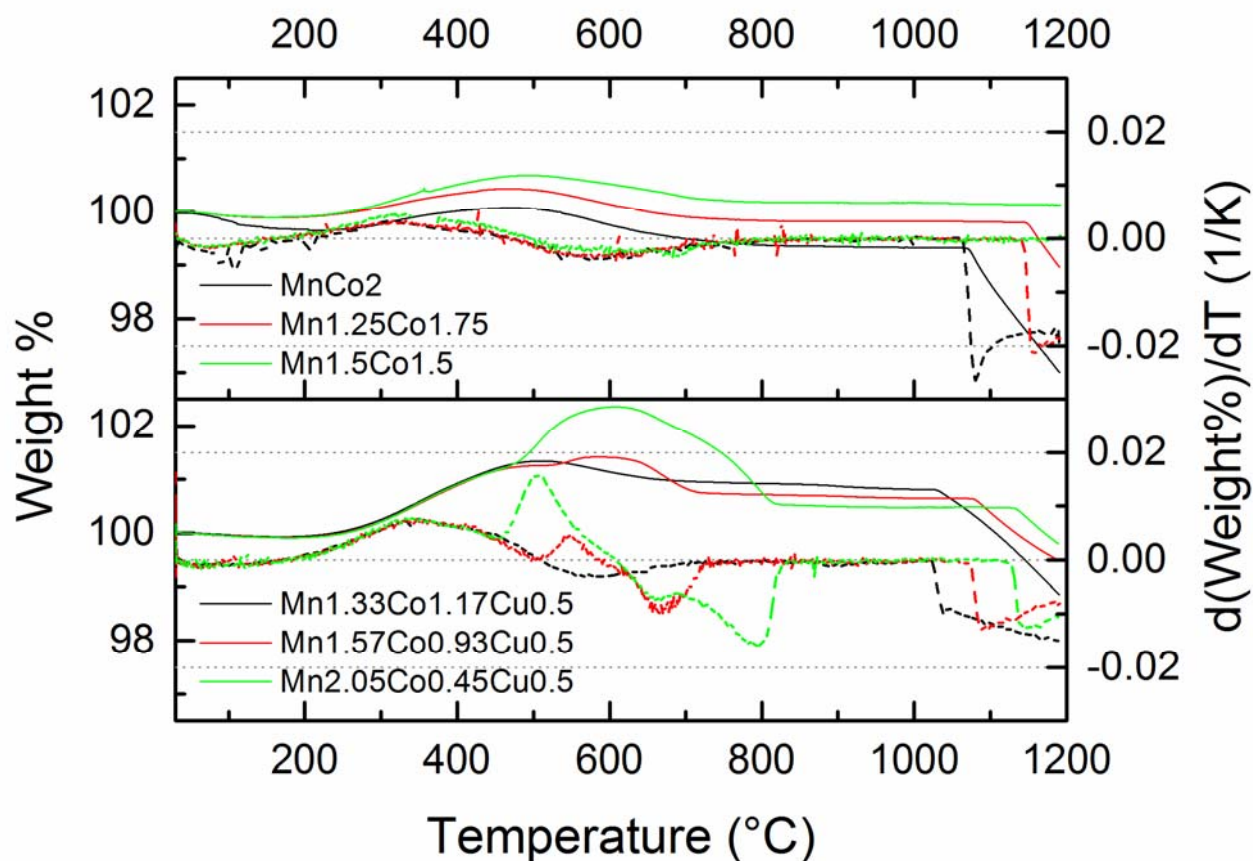
178 Raising the temperature, in the 500-700°C temperature range, the Mn-Co and Mn1.33Co1.17Cu0.5
 179 samples show a similar gradual weight loss, reaching a plateau for higher temperatures. In this
 180 temperature range, for the Mn-Co samples the reaction between the activated precursors is expected

181 [17]. The release of the extra oxygen content acquired during the previous weight acquisition step,
182 followed by an interval of weight stability, is compatible therefore with the reorganization of the
183 metastable oxidized lattices to form high temperature stable phases.

184 The Mn richest samples, i.e. $\text{Mn}_{1.57}\text{Co}_{0.93}\text{Cu}_{0.5}$ and $\text{Mn}_{2.05}\text{Co}_{0.45}\text{Cu}_{0.5}$, undergo instead a
185 further weight acquisition step before exhibiting weight loss. In our previous work we had observed
186 how the presence of Mn-rich unreacted spinels could lead to the oxidation of Mn_3O_4 to Mn_2O_3
187 during heating, and it is likely to ascribe this weight gain to a similar phenomenon. Raising further
188 the temperature, the oxidized compound reacts with the existing spinels, resulting in weight loss and
189 formation of spinel phases. The behaviour of the Cu-doped samples will be further investigated in
190 the next section by means of the outcome of in-situ high temperature XRD analysis.

191 Further heating over 1000°C leads to an additional weight loss phenomenon for all samples except
192 $\text{Mn}_{1.5}\text{Co}_{1.5}$. Regarding Mn-Co samples, it is known that at high temperature, a multi-phase
193 boundary between spinels and reduced Me^{II} oxide phases exists for Co-Mn oxide mixtures [4], with
194 equilibrium temperature increasing with Mn content. The absence of the weight loss phenomena for
195 the sample $\text{Mn}_{1.5}\text{Co}_{1.5}$ indicates for this composition a phase boundary temperature beyond
196 1200°C . In the case of Cu addition, a similar behaviour can be supposed, with a dual phase region
197 also for the mixed Cu-Mn-Co oxides. Unlike Mn-Co samples, the weight loss is observed for all the
198 compositions. Considering that the $\text{Mn}_{2.05}\text{Co}_{0.45}\text{Cu}_{0.5}$ sample is characterized by an approximate
199 4:1 Mn:Co ratio, it is evident that copper lowers significantly the dual phase region boundary
200 temperature.

201 During cooling, the high temperature weight loss phenomenon is recovered for all samples, and no
202 significant weight change phenomena can be observed.



203

204 *Fig. 2. Thermogravimetric curves as a function of temperature for the different samples; solid lines represent*
 205 *weight% change, dotted lines the derivative.*

206

207 To further investigate the behaviour of the Cu doped samples upon heating, in situ diffraction
 208 analyses were carried out on the ball-milled powders. High temperature patterns are reported in Fig.
 209 3.

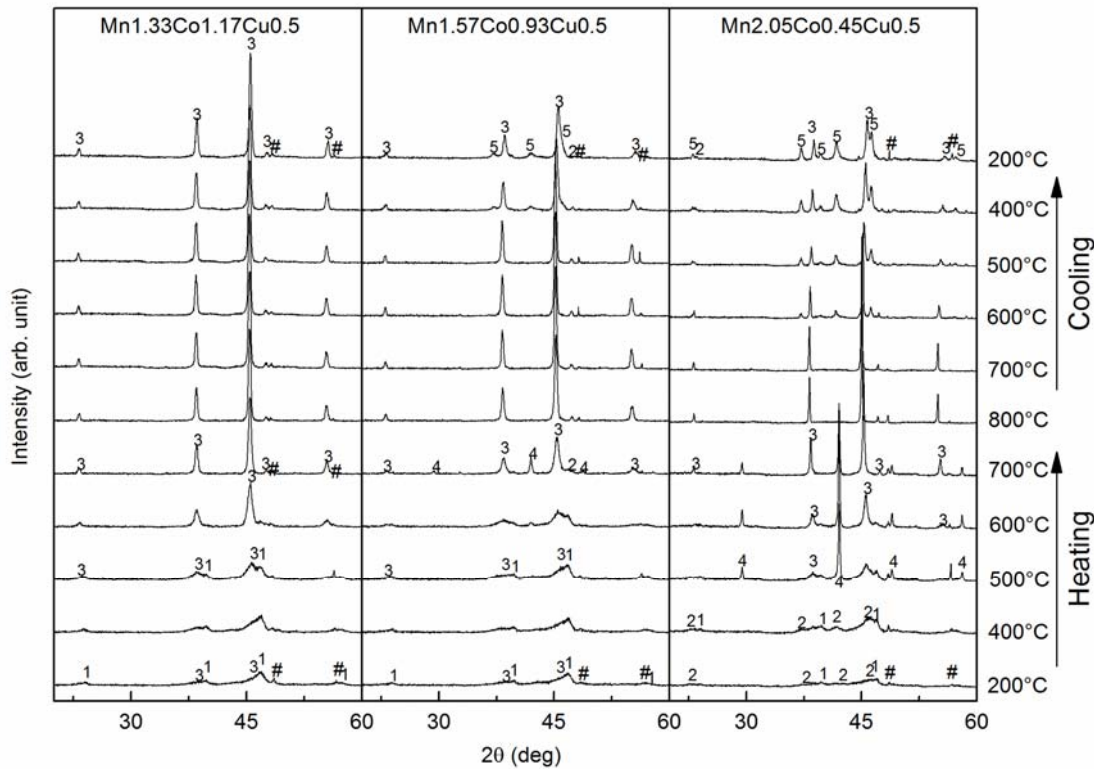
210 Starting from the Mn_{1.33}Co_{1.17}Cu_{0.5} sample, the pattern collected at 400°C is substantially
 211 similar to that acquired at room temperature, confirming that the oxidation phenomena observed
 212 with TGA measurements do not involve reactions or significant nucleation of new phases. The
 213 reaction between the activated precursors is instead evident at 500°C, where the nucleation of a
 214 cubic spinel phase occurs. Heating further, the reaction between the remaining precursors carries
 215 on, forming a single cubic spinel phase. The weight loss observed in the 500-700°C by
 216 thermogravimetric measurements can be associated therefore to the rearrangement of the metastable

217 oxidized lattice, resulting in the nucleation of the high temperature spinel. During cooling, no
218 structural changes are evident, showing that the examined composition is characterized by a single
219 phase nature in the ambient – 800°C temperature range.

220 The initial evolution of Mn_{1.57}Co_{0.93}Cu_{0.5} sample is similar, with the nucleation of a cubic spinel
221 phase in the 400°C-500°C interval. At 600°C reflections ascribable to the Mn₂O₃ phase (JCPDS
222 card n. 24-0508) are visible, explaining the thermogravimetric weight gain occurring in the 600-
223 700°C range. The growth of the spinel phase carries along with it the increase of peaks related to
224 this Mn-rich phase up to 700°C. Between 700°C and 800°C the rising spinel phase and Mn₂O₃
225 react, and the pattern collected at 800°C is ascribable to the presence of a single spinel phase.
226 During cooling, this phase is stable down to 500°C. At 400°C, reflections ascribable to a tetragonal
227 spinel phase similar to Mn₂CoO₄ (JCPDS 48-1548) appear, indicating the decomposition of the
228 high temperature cubic phase with the formation of a dual phase compound.

229 Regarding the Mn_{2.05}Co_{0.45}Cu_{0.5} sample, coherently with thermogravimetric results, nucleation
230 of large amounts of the oxidized Mn₂O₃ phase occur already at 500°C, along with the formation of
231 a cubic spinel phase. The transformation of Mn₃O₄ and Co₃O₄ precursor phases occurs between
232 500°C and 700°C, where only Mn₂O₃ and the spinel phase are visible. Raising the temperature,
233 Mn₂O₃ and the spinel phase react, and at 800°C the spinel phase formation is almost complete.
234 Similarly to what was observed for the Mn_{1.57}Co_{0.93}Cu_{0.5} sample, during cooling the segregation
235 of a tetragonal spinel phase is observed at a temperature value between 700°C and 600°C.

236



237

238 *Fig. 3: In situ X-ray diffraction patterns of a) Mn_{1.33}Co_{1.17}Cu_{0.5}, b) Mn_{1.57}Co_{0.93}Cu_{0.5} and c)*
 239 *Mn_{2.05}Co_{0.45}Cu_{0.5} samples milled for 10 hours collected at different temperatures (heating rate =*
 240 *10°C/min). Reflections ascribable to 1) Co₃O₄ 2) Mn₃O₄ 3) MnCo₂O₄ 4) Mn₂O₃ 5) Tetragonal mixed spinel*
 241 *phase and #) sample holder are indicated.*

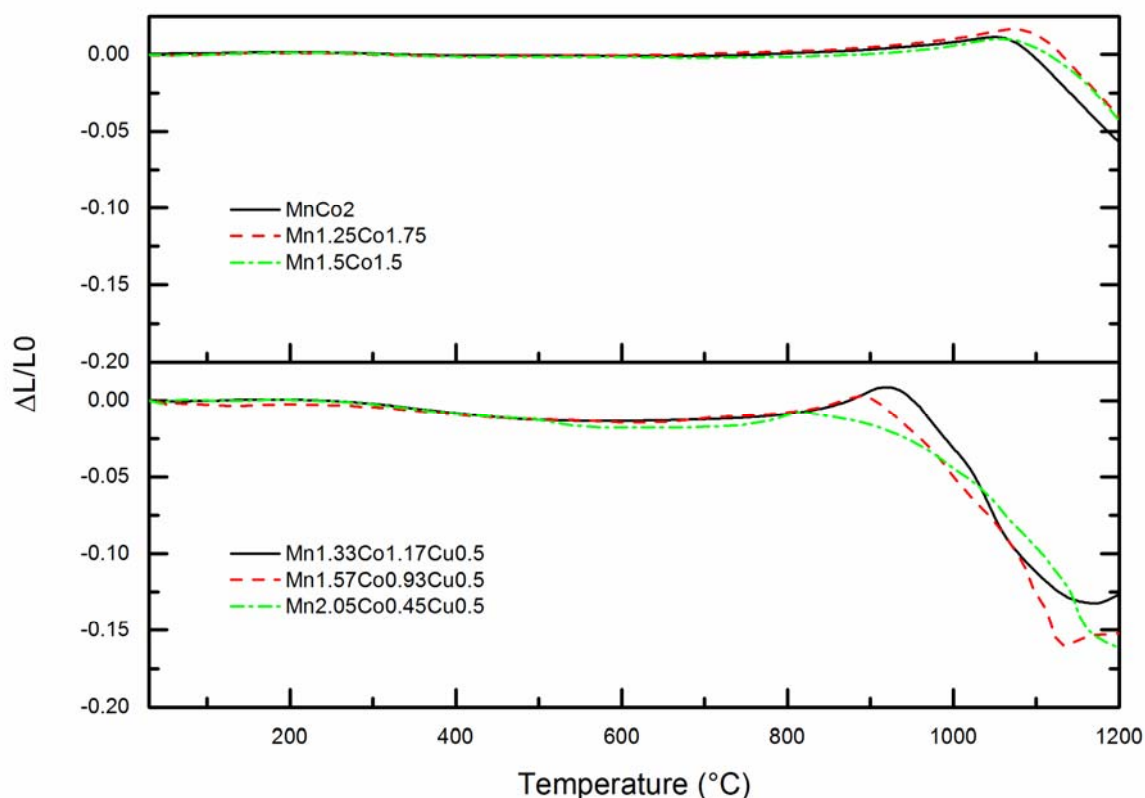
242

243 The evaluation of sintering behaviour was carried out on consolidated pellets prepared by uniaxial
 244 cold pressing. To compare sintering properties meaningfully, and ascribe differences to chemistry
 245 rather than to morphology of the powders, comparable pellet density is crucial. The geometric green
 246 densities are reported in Table 3: similar values are obtained for all the different samples, as
 247 expected from the processing of morphologically similar powders. The consolidated pellets were
 248 subjected to dilatometric measurements between room temperature and 1200°C, with a 5°C/min
 249 heating rate. Shrinkage curves are reported in Fig. 4. No significant differences can be observed
 250 between Mn-Co samples, with sintering temperatures of about 1040-1060°C and maximum
 251 densification rates at approximately 1150°C. Copper addition greatly enhances sintering behaviour:
 252 sintering temperatures are lowered to about 910°C, 870°C and 830°C respectively for

253 Mn_{1.33}Co_{1.17}Cu_{0.5}, Mn_{1.57}Co_{0.93}Cu_{0.5} and Mn_{2.05}Co_{0.45}Cu_{0.5}, and the shrinkage extent is
254 greatly increased with respect to Mn-Co samples. High temperature dilatation phenomena are
255 however visible in Mn_{1.33}Co_{1.17}Cu_{0.5} and Mn_{1.57}Co_{0.93}Cu_{0.5} curves. To further investigate
256 this phenomenon, a pellet obtained by pressing Mn_{1.33}Co_{1.17}Cu_{0.5} powder was heated in furnace
257 at 1200°C for 10 minutes and slowly cooled. The SEM image is reported in Fig. 5a. Significant
258 grain growth and inter-grain porosity can be observed, as well as the presence of an irregular and
259 corrugated Cu-rich phase. The observation of the samples clearly suggests a liquid phase sintering
260 at high temperature, most likely due to segregation and melting of the Cu-rich phase, that could
261 result in swelling phenomena [27]. The contemporary release of oxygen gas, as observed by
262 thermogravimetric analysis, when occurring in a highly packed structure could furthermore enhance
263 the expansion phenomena.

264 XRD analysis of the pellets after dilatometric measurements demonstrated in most cases secondary
265 phases in addition to the spinel. Differently from TGA measurements, the pelletized materials did
266 not recover the oxygen loss properly during cooling, probably due to higher packing of particles,
267 high crystal growth and subsequent reduced oxygen diffusion kinetics.

268



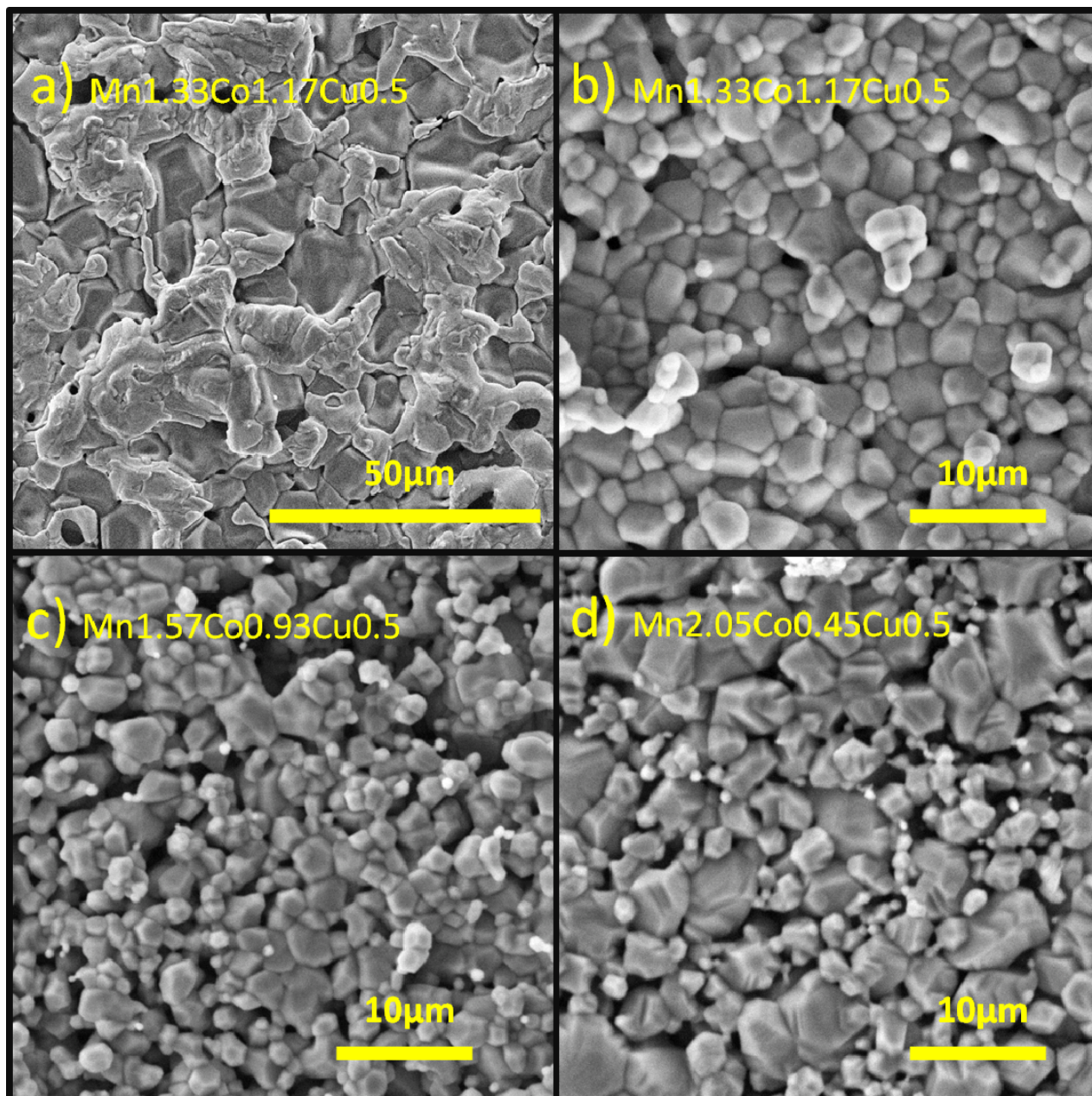
269

270 *Fig. 4. Dilatometric curves as a function of temperature of the different samples.*

271

272 The undesired phase segregation upon sintering at high temperature is an issue to precisely
 273 determine CTE and electrical properties of the material. Therefore, the sintering treatment of the
 274 pellets needed for dilatometry and Van der Pauw experiments was tailored. In the case of Mn-Co
 275 samples, it was not possible to reduce the temperature to avoid secondary phase formation, but a
 276 second dwell at lower temperature (i.e. 800°C) was successfully introduced to facilitate the spinel
 277 recovery. For MnCo₂ sample a further annealing (16h at 1000°C) was required to achieve single
 278 phase pellets, as observed for similar samples prepared with other synthesis routes [8]. For Mn-Co-
 279 Cu samples instead, the lower sintering temperature setup, as observed in dilatometric
 280 measurements, allowed to reduce the thermal treatment to 1000°C, avoiding segregation of Cu-rich
 281 phases and still obtaining sufficiently dense pellets. In Fig. 5b-d SEM images of the
 282 Mn_{1.33}Co_{1.17}Cu_{0.5}, Mn_{1.57}Co_{0.93}Cu_{0.5} and Mn_{2.05}Co_{0.45}Cu_{0.5} samples after sintering at
 283 1000°C are reported. A homogeneous morphology can be observed, characterized by significantly

284 lower crystal growth with respect to the 1200°C thermal treatment. In Table 3 a summary of the
285 performed thermal treatments and the geometrical density measured after sintering is reported. It
286 can be noted that Cu addition leads to densities comparable to Mn-Co samples even with a 200K
287 reduction in sintering temperature.
288



289

290 *Fig. 5: SEM images of samples heat treated at a)1200°C and b,c,d) 1000°C (see text for details).*

291

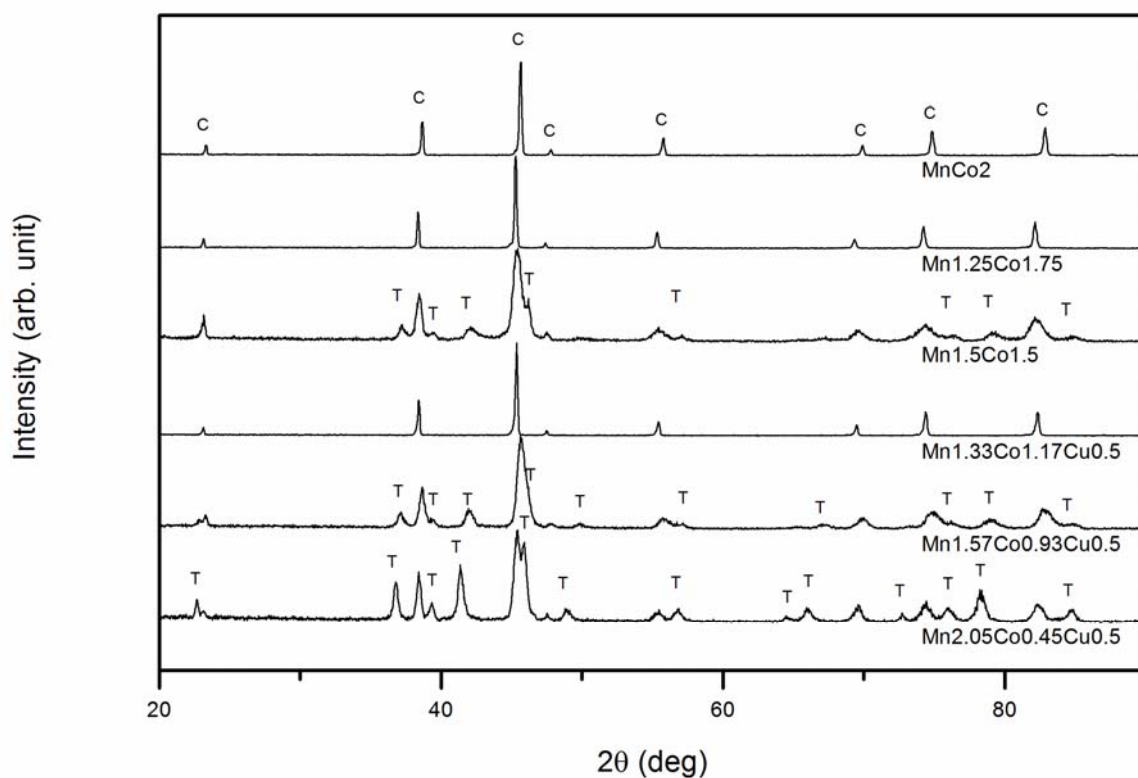
292 *Table 3: Sintering thermal treatments:*

Sample	Green density %	Sintering treatment	Sintered density %
MnCo2	66±1	4 h @1200°C + 4 h @800°C 16h @ 1000°C post sintering	93±1
Mn1.25Co1.75	67±1	4 h @1200°C + 4 h @800°C	93±1
Mn1.5Co1.5	67±1		95±2
Mn1.33Co1.17Cu0.5	65±1		97±1
Mn1.57Co0.93Cu0.5	64±1	4 h @1000°C + 4 h @800°C	97±2
Mn2.05Co0.45Cu0.5	65±1		97±2

293

294 In Fig. 6 X-Ray diffraction patterns of the sintered samples are reported. MnCo2 and
 295 Mn1.25Co1.75 show a pattern ascribable to a single cubic phase, with small shifts due to different
 296 Mn:Co ratio, while Mn1.5Co1.5 exhibits a mixture of a tetragonal and cubic spinels. These results
 297 are in agreement with the Mn-Co oxides phase diagram at room temperature. A single cubic phase
 298 is stable for high Co content (Co:Mn>1.3), a single tetragonal phase is obtained for high Mn content
 299 (Co:Mn<0.5), while for intermediate compositions, depending on the synthesis and cooling method,
 300 a mixture of the two phases or a single metastable tetragonal phase is observed[4,5]. Regarding Cu-
 301 Mn-Co samples, as observed by HT-XRD, Mn1.33Co1.17Cu0.5 is characterized by a single cubic
 302 phase, while raising Mn content peaks ascribable to a tetragonal spinel phase appear. Differently
 303 from Mn-Co composition, where Mn rich spinels exhibit a single tetragonal phase, copper addition
 304 enhances the cubic phase stability region, as evident by the phase composition of the
 305 Mn2.05Co0.45Cu0.5 sample, characterized by a mixture of cubic and tetragonal phases.

306



307

308 *Fig. 6. X-ray powder diffraction patterns of the samples after sintering treatment; C specify reflections*
 309 *ascribable to a cubic spinel phase, T to a tetragonal spinel phase.*

310

311 3.2. Thermal expansion

312 To evaluate the CTE of the different compositions, the sintered pellets were subjected to
 313 dilatometric analyses, and the obtained curves are reported in Fig. 7. Regarding Mn-Co samples, it
 314 can be observed that higher Co content induces higher expansion. MnCo_2 and $\text{Mn}_{1.25}\text{Co}_{1.75}$
 315 samples, characterized by a single phase in the whole examined temperature range, show a
 316 corresponding linear behaviour. $\text{Mn}_{1.5}\text{Co}_{1.5}$ curve shows instead a discontinuity in the 500-600°C
 317 temperature range, ascribable to the dual phase – single phase transition. Regarding copper addition,
 318 a similar behaviour can be observed: the dual-phase samples (those richest in Mn) exhibit a
 319 discontinuity in the 450-600°C temperature range and in the 600-750°C for the
 320 $\text{Mn}_{1.57}\text{Co}_{0.93}\text{Cu}_{0.5}$ and $\text{Mn}_{2.05}\text{Co}_{0.45}\text{Cu}_{0.5}$ samples respectively, most likely related to the
 321 dual-single phase transition occurring in these temperature intervals.

322 Average CTE values have been calculated between room temperature and 800°C, and are reported
323 in Table 4. Among the considered composition, Mn_{1.57}Co_{0.93}Cu_{0.5} and Mn_{1.25}Co_{1.75} exhibit
324 the highest compatibility with thermal expansion of ferritic stainless steels ($11-13 \cdot 10^{-6} \text{ K}^{-1}$ [28]). To
325 evaluate how the different Mn:Co ratio and Cu addition influence CTE, in Fig. 8 are reported the
326 CTE values at 800°C versus the cobalt content for the different samples. Regarding Mn-Co
327 composition, a clear linear trend can be observed between the composition and CTE values. Also
328 for Cu doped samples an analogue behaviour can be observed when changing Mn:Co ratio, and Cu
329 addition does not affect significantly this trend but rather induces a shift of the curve toward higher
330 CTEs.

331 The observed behaviour can be ascribed to the chemical differences between the samples
332 considering lattice sites occupations and atoms valence. In particular, thermal expansion of mixed
333 metal spinels can be related to the composition principally via the occupation of octahedral sites
334 [29], where compounds characterized by high valence differences possess higher CTE.

335 Mn-Co spinels are characterized by a preferential occupation of tetrahedral sites by Co^{II} atoms. Co^{II},
336 Co^{III}, Mn^{III} and Mn^{IV} occupy octahedral sites, with Co^{II} and Mn^{IV} amounts related to electro-
337 neutrality constraints [30]. In the $1:1 \leq \text{Co}:\text{Mn} \leq 2:1$ compositional range, the increase of Co promotes
338 an increase of Co^{II}, Co^{III} and Mn^{IV} species at the expense of Mn^{III} atoms[31]. Increasing Co content
339 in this composition range will cause therefore higher inhomogeneity, theoretically raising CTE, in
340 agreement with our results.

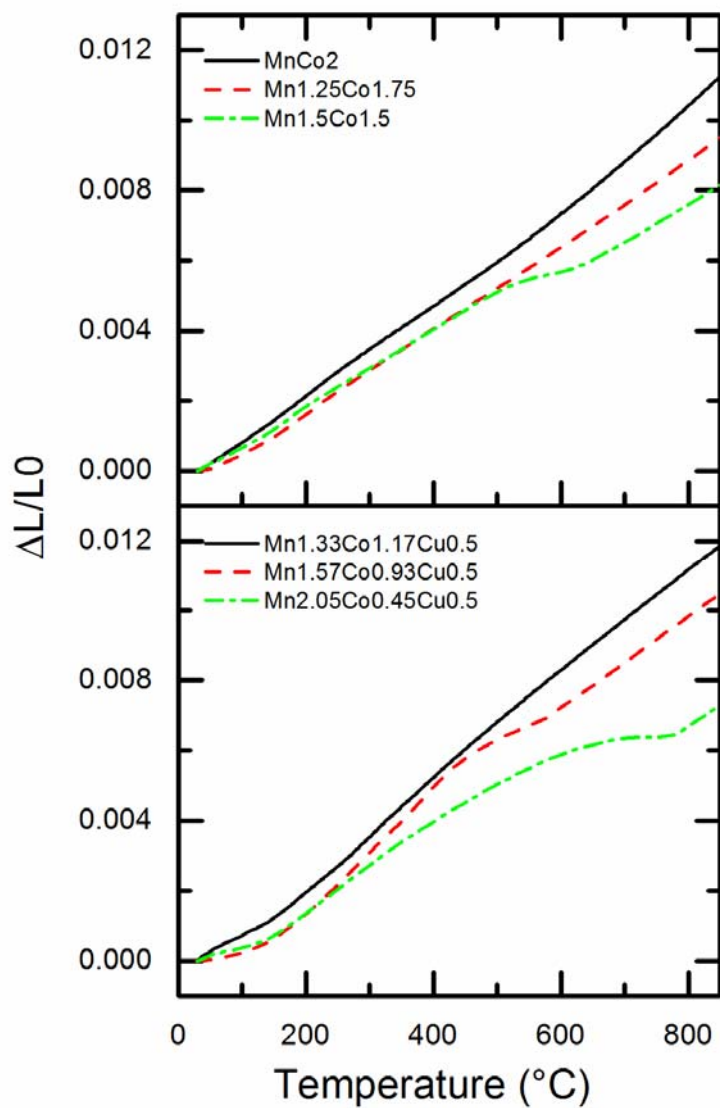
341 In mixed Cu-Co-Mn compounds instead, Cu^I/Cu^{II} species tend to occupy tetrahedral sites
342 preferentially over Co^{II} atoms, leading to an enrichment of Co^{II}/Co^{III} pairs in octahedral sites [32].
343 Furthermore, the presence of Cu^I atoms promotes Mn^{III} oxidation to Mn^{IV} to maintain charge
344 neutrality. Valence differences are therefore increased with copper doping, enhancing CTE.

345

346 Table 4. Thermal expansion coefficient at 800°C measured for the different samples:

Sample	CTE @800°C ($\cdot 10^{-6} \text{ K}^{-1}$)
MnCo2	13.5±0.1
Mn1.25Co1.75	11.5±0.1
Mn1.5Co1.5	9.7±0.1
Mn1.33Co1.17Cu0.5	14.5±0.1
Mn1.57Co0.93Cu0.5	12.7±0.1
Mn2.05Co0.45Cu0.5	8.5±0.1

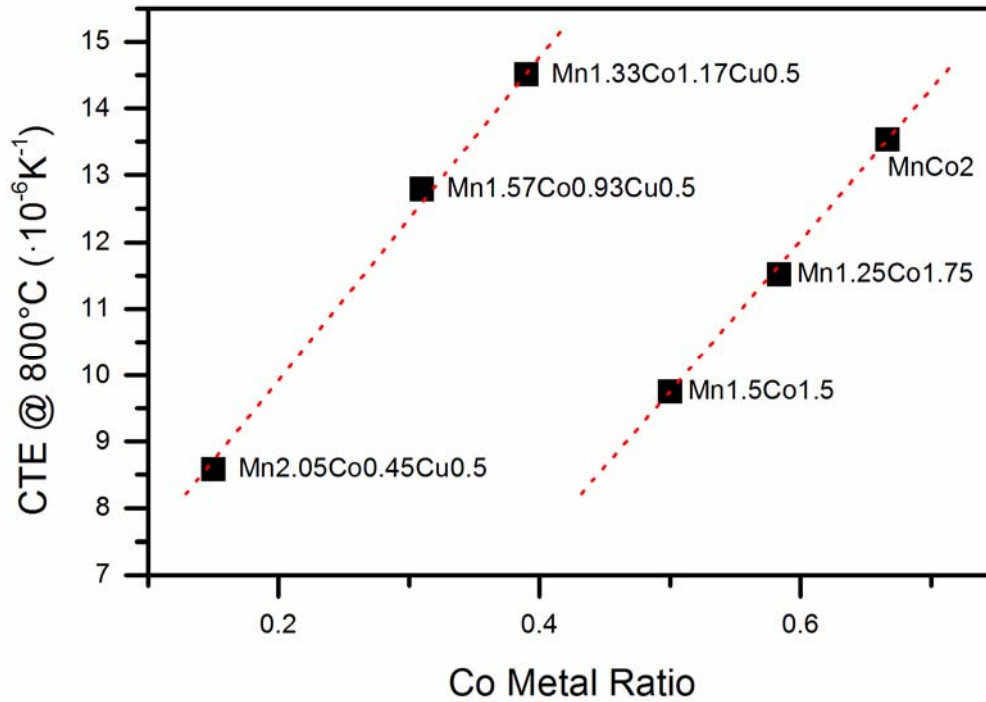
347



348

349 Fig. 7. Thermal expansion curves of the sintered samples.

350



351

352 *Fig. 8. Coefficient of thermal expansion calculated at 800°C as a function of the sample composition.*

353

354 3.3. Electrical conductivity

355 Electrical conductivity measurement was carried out by means of the Van der Pauw method in the
356 temperature range 500-800°C. In Fig. 9 are reported Arrhenius plots.

357 MnCo₂, Mn_{1.25}Co_{1.75} and Mn_{1.33}Co_{1.17}Cu_{0.5} samples exhibit a linear behaviour through all the
358 examined range, as expected by their single phase nature. On the contrary, samples characterized
359 by dual to single phase transitions show slope changes in their linear trend, at temperatures coherent
360 with the discontinuities observed during dilatometric measurements. From the single-phase region
361 of the Arrhenius plots, the activation energies were calculated and are reported in Table 5. Mn-Co
362 samples exhibit comparable values of about 0.5eV, while Cu addition lowers significantly in all
363 cases the activation energy to about 0.3eV.

364 To better evaluate how Mn:Co ratio and Cu addition affect electrical properties, in Fig. 10 are
365 reported conductivity values measured at 800°C versus cobalt content. The MnCo₂ sample is

366 characterized by a conductivity value of about 80S/cm, and a decreasing trend can be observed
367 increasing Mn content. A similar decrease in conductivity with Mn content can be observed for the
368 Cu doped samples as well. On the other hand, Cu addition increases electrical conductivity, with the
369 Mn_{1.33}Co_{1.17}Cu_{0.5} sample characterized by a conductivity value of about 125S/cm.

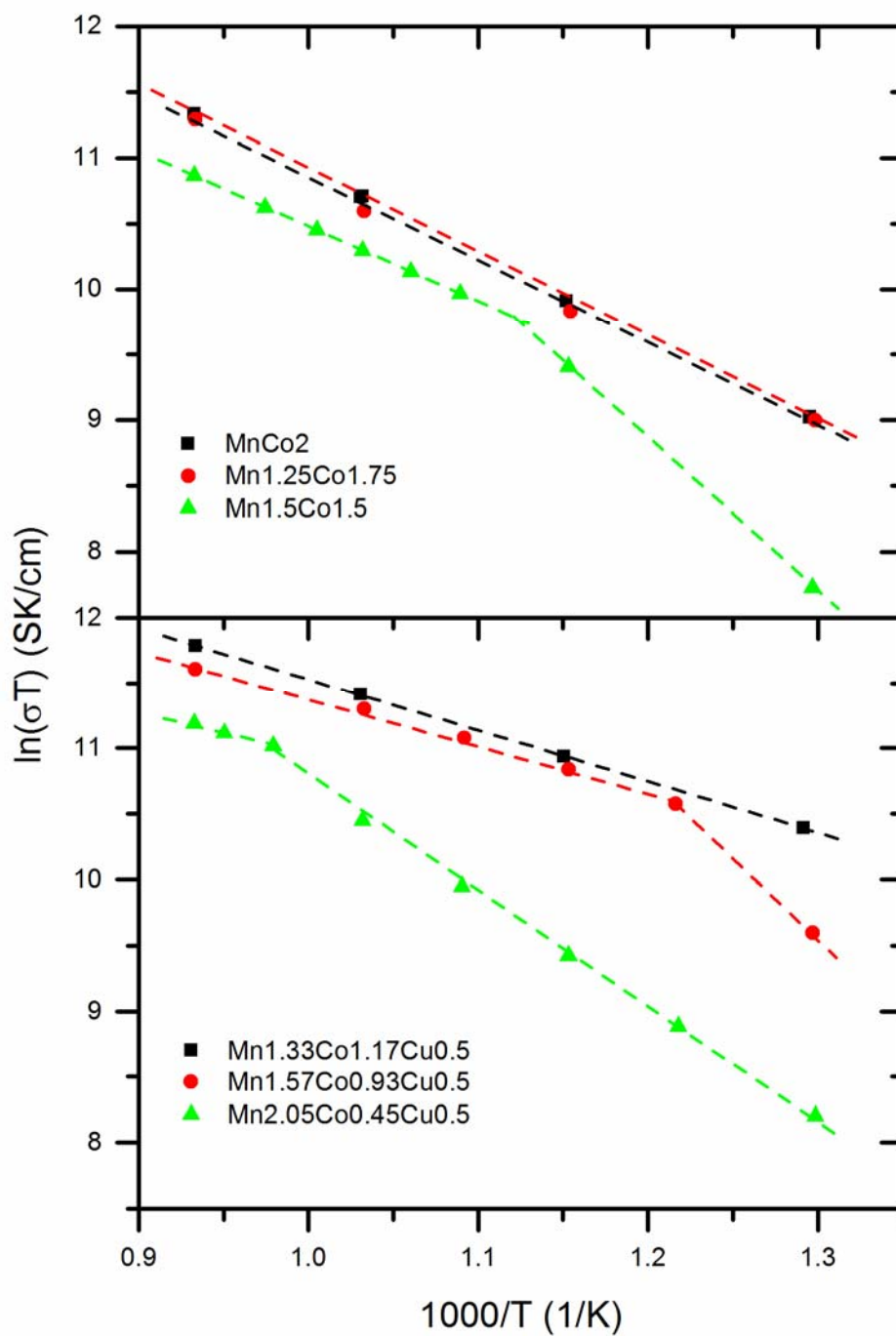
370 In such spinel systems, the conductivity behaviour is usually explained with a small polaron
371 hopping mechanism between mixed valence elements on octahedral sites, and in Mn-Co oxides it is
372 usually related to Co^{II}/Co^{III} and Mn^{III}/Mn^{IV} pairs [3,30,31]. The Co^{II}/Co^{III} and Mn^{III}/Mn^{IV}
373 concentration ratio affects therefore conductivity properties, Co^{III} and Mn^{III} being the most common
374 species in octahedral sites. The observed trend for Mn-Co samples is in agreement with previous
375 findings, and is related to the maximum concentration of Co^{II} and Mn^{IV} species for compositions
376 with Mn:Co \approx 2:1 [31]. The similar increasing trend here observed for the Cu-doped samples
377 suggests that similar phenomena can be accounted for also in Cu-Mn-Co samples. The significant
378 increase of conductivity in Cu samples with respect to Mn-Co compounds can be instead due to
379 multiple mechanisms. Copper addition in mixed Mn-Co spinels occurs with preferential occupation
380 of tetrahedral sites of the spinel lattice by Cu^I and Cu^{II} species, that promotes Mn^{III} oxidation to
381 Mn^{IV} to maintain charge neutrality. As a consequence, Cu introduction increases active pairs
382 concentration and therefore electrical conductivity [32]. Tetrahedral Cu ions could furthermore
383 contribute indirectly to electrical conductivity, through mediation of charge transfer mechanisms
384 between near but not adjacent Mn atoms, as observed in Ni-Cu manganite spinels [33].

385

386 *Table 5. Activation energy calculated from the Arrhenius plot of 10 hours milled samples:*

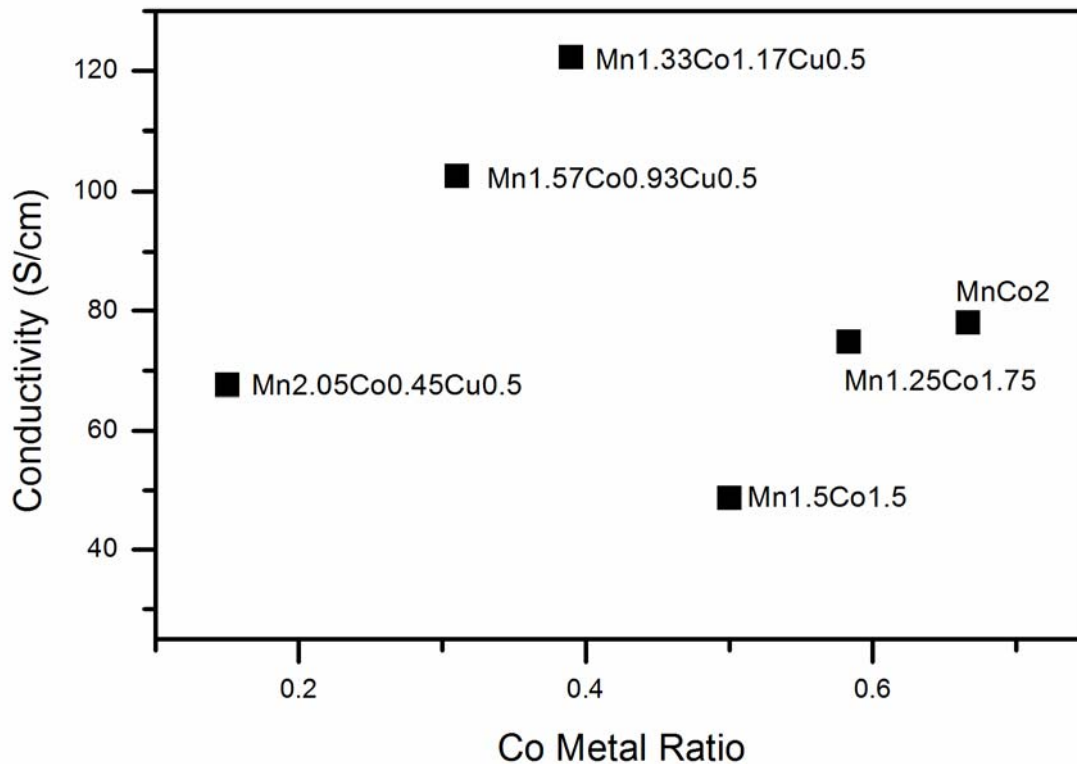
Sample	Temperature range (°C)	Ea (eV)
MnCo ₂	500-800	0.55±0.02
Mn _{1.25} Co _{1.75}	500-800	0.54±0.04

Mn1.5Co1.5	650-800	0.49±0.02
Mn1.33Co1.17Cu0.5	500-800	0.34±0.02
Mn1.57Co0.93Cu0.5	600-800	0.32±0.03
Mn2.05Co0.45Cu0.5	750-800	0.32±0.04



387

388 *Fig. 9: Arrhenius plots of electrical conductivity measured for the different samples.*



390

391 *Fig. 10. Conductivity values measured at 800°C as a function of the sample composition.*

392

393 4. Conclusions

394 Different Mn-Co and Cu-Mn-Co spinels were synthesised in order to evaluate the effect of Mn:Co
 395 ratio and copper addition on sintering behaviour, thermal expansion and electrical conductivity.

396 A High Energy Ball Milling treatment of oxide powders was utilized to produce highly reactive
 397 metastable multi-phase compounds that easily homogenize when brought to intermediate
 398 temperature ($T < 800^\circ\text{C}$) to form the equilibrium products. The influence of the different spinel
 399 compositions was observed on high temperature ($T > 1000^\circ\text{C}$) behaviour of each compound,
 400 evidencing that Cu decreases the spinel stability region. Thermogravimetric and in situ high
 401 temperature XRD analysis allowed to observe for the examined Cu-Mn-Co compositions a single
 402 cubic phase stable at high operating temperature (800°C). Different Mn:Co ratios did not lead to

403 significant differences in sintering behaviour, while Copper addition proved to be highly effective
404 in reducing sintering temperature and obtaining high densities.

405 Dilatometry experiments performed on sintered pellets allowed to observe a simple relation
406 between CTE and composition: CTE similarly increases with cobalt content, both in Mn-Co and
407 Cu-Mn-Co samples, with Cu doped samples characterized by higher CTE values.. A similar relation
408 could be observed also from electrical conductivity, being enhanced (up to 125S/cm) by Cu
409 addition and high cobalt content. The thermal expansion and electrical conductivity of Mn-Co
410 spinels can thus be tuned by varying stoichiometry.

411 Despite the best coating spinel composition cannot be given in absolute, because depending on the
412 interconnector alloy (and its CTE) and on the deposition process used, it is possible to state that the
413 fine tuning of stoichiometry is the strategy to design an ideal coating spinel. Cu addition to spinels
414 characterized by the opportune Mn-Co ratio represent a further possibility to optimize a material
415 capable to satisfy the properties required by the interconnect coating with the advantage of limiting
416 the use of an expensive and toxic element like Co.

417

418 Acknowledgments

419 This work is supported by the FCH JU within the project SCORED 2:0 under contract. 325331. The
420 authors wish to thank Dr. Claudia Paoletti for the technical support and useful discussions.

421

422 Bibliography

- 423 [1] N. Shaigan, W. Qu, D.G. Ivey, W. Chen, A review of recent progress in coatings, surface
424 modifications and alloy developments for solid oxide fuel cell ferritic stainless steel
425 interconnects, *J. Power Sources*. 195 (2010) 1529–1542.
426 doi:10.1016/j.jpowsour.2009.09.069.
- 427 [2] J. Wu, X. Liu, Recent development of SOFC metallic interconnect, *J. Mater. Sci. Technol.* 26
428 (2010) 293–305. doi:10.1016/S1005-0302(10)60049-7.
- 429 [3] A. Petric, H. Ling, Electrical Conductivity and Thermal Expansion of Spinel at Elevated
430 Temperatures, *J. Am. Ceram. Soc.* 90 (2007) 1515–1520. doi:10.1111/j.1551-
431 2916.2007.01522.x.
- 432 [4] E. Aukrust, A. Muan, Phase Relations in the System Cobalt Oxide-Manganese Oxide in Air,
433 *J. Am. Ceram. Soc.* 46 (1963) 511–511. doi:10.1111/j.1151-2916.1963.tb13790.x.
- 434 [5] Y.V. Golikov, S.Y. Tubin, V.P. Barkhatov, V.F. Balakirev, Phase diagrams of the Co-Mn-O
435 system in air, *J. Phys. Chem. Solids*. 46 (1985) 539–544. doi:10.1016/0022-3697(85)90215-
436 X.
- 437 [6] X. Xin, S. Wang, Q. Zhu, Y. Xu, T. Wen, A high performance nano-structure conductive
438 coating on a Crofer22APU alloy fabricated by a novel spinel powder reduction coating
439 technique, *Electrochem. Commun.* 12 (2010) 40–43. doi:10.1016/j.elecom.2009.10.031.
- 440 [7] Y. Xu, Z. Wen, S. Wang, T. Wen, Cu doped Mn–Co spinel protective coating on ferritic
441 stainless steels for SOFC interconnect applications, *Solid State Ionics*. 192 (2011) 561–564.
442 doi:10.1016/j.ssi.2010.05.052.
- 443 [8] Y. Liu, J.W. Fergus, K. Wang, C. Dela Cruz, Crystal Structure, Chemical Stabilities and
444 Electrical Conductivity of Fe-Doped Manganese Cobalt Spinel Oxides for SOFC
445 Interconnect Coatings, *J. Electrochem. Soc.* 160 (2013) F1316–F1321.

- 446 doi:10.1149/2.114311jes.
- 447 [9] B.-K. Park, J.-W. Lee, S.-B. Lee, T.-H. Lim, S.-J. Park, C.-O. Park, R.-H. Song, Cu- and Ni-
448 doped $\text{Mn}_{1.5}\text{Co}_{1.5}\text{O}_4$ spinel coatings on metallic interconnects for solid oxide fuel cells, *Int.*
449 *J. Hydrogen Energy*. 38 (2013) 12043–12050. doi:10.1016/j.ijhydene.2013.07.025.
- 450 [10] Z. Yang, G. Xia, S.P. Simner, J.W. Stevenson, Thermal Growth and Performance of
451 Manganese Cobaltite Spinel Protection Layers on Ferritic Stainless Steel SOFC
452 Interconnects, *J. Electrochem. Soc.* 152 (2005) A1896. doi:10.1149/1.1990462.
- 453 [11] Z. Yang, G.-G. Xia, X.-H. Li, J.W. Stevenson, $(\text{Mn},\text{Co})_3\text{O}_4$ spinel coatings on ferritic
454 stainless steels for SOFC interconnect applications, *Int. J. Hydrogen Energy*. 32 (2007)
455 3648–3654. doi:10.1016/j.ijhydene.2006.08.048.
- 456 [12] K. Wang, Y. Liu, J.W. Fergus, Interactions Between SOFC Interconnect Coating Materials
457 and Chromia, *J. Am. Ceram. Soc.* 94 (2011) 4490–4495. doi:10.1111/j.1551-
458 2916.2011.04749.x.
- 459 [13] M.Y. Yoon, E.J. Lee, R.H. Song, H.J. Hwang, Preparation and properties of a MnCo_2O_4 for
460 ceramic interconnect of solid oxide fuel cell via glycine nitrate process, *Met. Mater. Int.* 17
461 (2011) 1039–1043. doi:10.1007/s12540-011-6025-5.
- 462 [14] Y. Liu, J.W. Fergus, C. Dela Cruz, Electrical properties, cation distributions, and thermal
463 expansion of manganese cobalt chromite spinel oxides, *J. Am. Ceram. Soc.* 96 (2013) 1841–
464 1846. doi:10.1111/jace.12254.
- 465 [15] G. Chen, X. Xin, T. Luo, L. Liu, Y. Zhou, C. Yuan, C. Lin, Z. Zhan, S. Wang,
466 $\text{Mn}_{1.4}\text{Co}_{1.4}\text{Cu}_{0.2}\text{O}_4$ spinel protective coating on ferritic stainless steels for solid oxide fuel
467 cell interconnect applications, *J. Power Sources*. 278 (2015) 230–234.
468 doi:10.1016/j.jpowsour.2014.12.070.
- 469 [16] J. Xiao, W. Zhang, C. Xiong, B. Chi, J. Pu, L. Jian, Oxidation of $\text{MnCu}_{0.5}\text{Co}_{1.5}\text{O}_4$ spinel

- 470 coated SUS430 alloy interconnect in anode and cathode atmospheres for intermediate
471 temperature solid oxide fuel cell, *Int. J. Hydrogen Energy*. 40 (2015) 1868–1876.
472 doi:10.1016/j.ijhydene.2014.11.124.
- 473 [17] A. Masi, M. Bellusci, M. Carlini, S.J. McPhail, F. Padella, P. Reale, Mechanochemical
474 Processing of Mn and Co Oxides: An Alternative Way to Synthesize Mixed Spinel for
475 Protective Coating, *J. Am. Ceram. Soc.* 99 (2016) 308–314. doi:10.1111/jace.13863.
- 476 [18] P. Baláž, M. Achimovičová, M. Baláž, P. Billik, Z. Cherkezova-Zheleva, J.M. Criado, F.
477 Delogu, E. Dutková, E. Gaffet, F.J. Gotor, R. Kumar, I. Mitov, T. Rojac, M. Senna, A.
478 Streletskii, K. Wieczorek-Ciurowa, Hallmarks of mechanochemistry: from nanoparticles to
479 technology, *Chem. Soc. Rev.* 42 (2013) 7571. doi:10.1039/c3cs35468g.
- 480 [19] F. Delogu, L. Schiffini, G. Cocco, The invariant laws of the amorphization processes by
481 mechanical alloying, *Philos. Mag. A*. 81 (2001) 1917–1937.
482 doi:10.1080/01418610010019107.
- 483 [20] A. Boschetto, M. Bellusci, A. La Barbera, F. Padella, F. Veniali, Kinematic observations and
484 energy modeling of a Zoz Simoloyer high-energy ball milling device, *Int. J. Adv. Manuf.*
485 *Technol.* 69 (2013) 2423–2435. doi:10.1007/s00170-013-5201-9.
- 486 [21] N. Burgio, A. Iasonna, M. Magini, S. Martelli, F. Padella, Mechanical alloying of the Fe–Zr
487 system. Correlation between input energy and end products, *Nuovo Cim. D*. 13 (1991) 459–
488 476. doi:10.1007/BF02452130.
- 489 [22] ICPDS.ICDD, -, PCPDF-WIN Version 2.01. (1998).
- 490 [23] S. Brunauer, P.H. Emmett, E. Teller, Adsorption of Gases in Multimolecular Layers, *J. Am.*
491 *Chem. Soc.* 60 (1938) 309–319. doi:10.1021/ja01269a023.
- 492 [24] L.J. van der Pauw, A method of measuring the resistivity and Hall coefficient on lamellae of
493 arbitrary shape, *Philips Tech. Rev.* 20 (1958) 220–224.

- 494 [25] G.C. Wood, T. Hodgkiess, The Hardness of Oxides at Ambient Temperatures, Mater. Corros.
495 Und Korrosion. 23 (1972) 766–773. doi:10.1002/maco.19720230905.
- 496 [26] B. Gillot, DTG Curves of Selective Oxidation of Submicrometer Mixed Valency Spinel:
497 Data Table for the Oxidation Temperature of Transition Metals and Its Relation to the
498 Cation-Oxygen Distance, J. Solid State Chem. 113 (1994) 163–167.
499 doi:10.1006/jssc.1994.1355.
- 500 [27] R.M. German, P. Suri, S.J. Park, Review: Liquid phase sintering, J. Mater. Sci. 44 (2009) 1–
501 39. doi:10.1007/s10853-008-3008-0.
- 502 [28] Z. Yang, K.S. Weil, D.M. Paxton, J.W. Stevenson, Selection and Evaluation of Heat-
503 Resistant Alloys for SOFC Interconnect Applications, J. Electrochem. Soc. 150 (2003)
504 A1188. doi:10.1149/1.1595659.
- 505 [29] G. Bayer, Thermal expansion of oxide compounds with spinel structure, Thermochem. Acta.
506 3 (1972) 421–426. doi:10.1016/0040-6031(72)85001-9.
- 507 [30] H. Bordeneuve, A. Rousset, C. Tenailleau, S. Guillemet-Fritsch, Cation distribution in
508 manganese cobaltite spinels $\text{Co}_{3-x}\text{Mn}_x\text{O}_4$ ($0 \leq x \leq 1$) determined by thermal analysis, J.
509 Therm. Anal. Calorim. 101 (2010) 137–142. doi:10.1007/s10973-009-0557-7.
- 510 [31] H. Bordeneuve, C. Tenailleau, S. Guillemet-Fritsch, R. Smith, E. Suard, A. Rousset,
511 Structural variations and cation distributions in $\text{Mn}_{3-x}\text{Co}_x\text{O}_4$ ($0 \leq x \leq 3$) dense ceramics using
512 neutron diffraction data, Solid State Sci. 12 (2010) 379–386.
513 doi:10.1016/j.solidstatesciences.2009.11.018.
- 514 [32] P. a. Wright, S. Natarajan, J.M. Thomas, P.L. Gai-Boyes, Mixed-metal amorphous and spinel
515 phase oxidation catalysts: characterization by x-ray diffraction, x-ray absorption, electron
516 microscopy, and catalytic studies of systems containing copper, cobalt, and manganese,
517 Chem. Mater. 4 (1992) 1053–1065. doi:10.1021/cm00023a024.

518 [33] E. Elbadraoui, Cation distribution and mechanism of electrical conduction in nickel-copper
519 manganite spinels, *Solid State Ionics*. 93 (1997) 219–225. doi:10.1016/S0167-
520 2738(96)00559-0.

521